Facile Synthesis of Nanosheet-like CuO Film and its Potential Application as a High-Performance Pseudocapacitor Electrode

Assumpta C. Nwanya[a,b], Daniel Obi[c], Kenneth I. Ozoemena[d,e], Rose U. Osuji[b,f,g], Chawki Awada[c], Andreas Ruediger[c], Malik Maaza[f,g], Federico Rosei[c], Fabian I. Ezema[b,e,g,*]

[a] National Centre for Energy Research and Development, University of Nigeria Nsukka, Nigeria
[b] Department of Physics and Astronomy, University of Nigeria Nsukka, Nigeria
[c] INRS Centre for Energy, Materials and Telecommunications and UNESCO Chair in Materials and Technologies for Energy Conversion, Saving and Storage, 1650, Boulevard Lionel-Boulet, Varennes, QC, J3 X1S2, Canada
[d] Energy Materials, Materials Science & Manufacturing, Council for Scientific & Industrial Research (CSIR), Pretoria, 0001, South Africa
[e] Molecular Sciences Institute, School of Chemistry, University of the Witwatersrand, Johannesburg 2050, South Africa
[f] Nanosciences African Network (NANOAFNET), iThemba LABS-National Research Foundation, 1 Old Faure road, Somerset West 7129, P.O. Box 722, Somerset West, Western Cape Province, South Africa
[g] UNESCO-UNISA Africa Chair in Nanosciences/Nanotechnology, College of Graduate Studies, University of South Africa (UNISA), Muckleneuk ridge, P.O. Box 392, Pretoria, South Africa,

ABSTRACT

We describe the chemical synthesis of binderless and surfactant free CuO films for pseudocapacitive applications. Nanosheet-like and nanorod-like CuO films are deposited on indium tin oxide (ITO) substrates using the successive ionic layer adsorption and reaction (SILAR) approach. The nanostructured CuO shows uniform surface morphology and uniform pore distribution with average grain sizes in the range $30 - 50\,nm$ and average pore size of 12.0 and 12.5 nm for 10 and for 40-cycles respectively, as estimated from AFM imaging. The electrochemical properties are characterized by cyclic voltammetry (CV), galvanostatic charge-discharge (GCD) and electrochemical impedance spectroscopy (EIS). The highest specific capacitance of 566.33 Fg^{-1} is obtained for as low as 10-cycle film at a scan rate of $5\,mVs^{-1}$. The long term stability tests by continuous GCD, indicates that there is no degradation after 1000 cycles with the film yielding 100% coulombic efficiency. This indicates a high stability of the synthesized CuO films. Hence, the developed nanostructured CuO film electrodes exhibit excellent properties for use as supercapacitors.

© 2016 Elsevier Ltd. All rights reserved.

1. Introduction

The increasing need for cost-effective and environmentally friendly energy for the world's growing population has led to intensive research for efficient energy storage systems [1]. In particular, due to their intermittency, the grand challenge for most renewable energy systems, such as e.g. wind power and solar power, is storage. High energy, high power density and fast availability are the major requirements of a storage device. Such needs are particularly pressing in rural areas, in which there is no decentralized energy distribution (i.e. typical electrical grids that are pervasive in developed countries). The combination of renewable energy technologies and improved energy storage devices is therefore expected to have a major impact in the developing world [2,3].

An electrochemical capacitor is an energy storage device which exhibits several advantages compared to batteries, such as high power densities ($10\,kW\,kg^{-1}$), moderate energy densities ($5\,Wh\,kg^{-1}$), and long cycle life ($>10^4$ cycles) [4]. These properties make them suitable for applications in a variety of fields such as consumer electronics and hybrid electric vehicles [5]. Since the energy stored in a capacitor is proportional to its surface area, the concept behind supercapacitors is to exploit nanostructured materials, which are highly porous and therefore have a high surface to volume ratio [6]. Electrochemical capacitors are categorized into two types: (i) supercapacitors also known as ultracapacitors or electric double layer capacitors (EDLC) (which store charge via the electric double layer or non-redox process) and (ii) pseudocapacitors (which store charge mainly via the redox process) [7–10]. Carbonaceous materials like activated carbon,

* Corresponding author. Tel.: +234 8036239214.
E-mail addresses: fabian.ezema@unn.edu.ng, fiezema@yahoo.com (F.I. Ezema).

mesoporous carbon, carbon nanotubes (CNTs), graphene etc. [11–15] that exhibits EDLC characteristics and their composites [16–19] have been used as electrode materials in supercapacitors due to their large specific surface area. However, the electrochemical capacitance performance of these carbonaceous materials does not meet the rapidly increasing demand for high-power and energy densities [20].

Transition metal oxides/hydroxides that store their charges by pseudo capacitance have also been considered as an alternative to carbon electrodes in supercapacitors [8,21–30]. Among these, the most widely investigated is ruthenium oxide (RuO_2), which has been shown to give appreciable specific capacitance of up to 1500 Fg^{-1} over a wide potential range of 1.4 V [31–33]. However, its commercial application is limited due to high cost and high toxicity. Several low-cost metal oxides such as NiO, Co_xO_x, $Ni(OH)_2$, Mn_xO_x, Cu_xO_x have also been extensively studied as potential materials for pseudo-capacitors, with the aim of reducing costs. Among the transition metal oxides, CuO is considered as a good electrode material for use in pseudocapacitors due to its low cost of synthesis, environmental friendliness and good potential storage capability [34]. Hence, many studies at 3-electrode configurations have been undertaken to improve its specific capacitance and stability for application in pseudocapacitors. To improve the psuedocapacitive properties of CuO, Yu et al. [35] synthesized nanostructured CuO directly on a Cu substrate and the as-prepared CuO yielded a capacitance of 348 Fg^{-1} at 1 Ag^{-1}. Dubal et al. [27,36,37] fabricated nanosheets, micro rose-like, and nanosheet clusters of nanostructures of copper oxide in the presence of different surfactants and obtained specific capacitance in the range of 110–400 F g^{-1}, depending on the surfactant and the scan rate in a 3-electrode configuration.

The electrochemical performance of electrode materials is highly dependent on their nanoscale structure, namely particle size, surface area, pore volume and crystallinity [4,20,34]. These features in turn depend on the deposition methods and parameters such as temperature, pH, precursor concentration, etc. Numerous methods such as electro-deposition, molten salt, RF magnetron, chemical bath deposition, hydrothermal method [23,37–42] have been used to deposit CuO and its mixed oxides for energy storage applications. Most of these methods have significant drawbacks such as high temperature requirements, long deposition time and involve multiple steps. Hence, there is a need to use cost effective, binder-free, additive-free, low temperature, and easy scalability for the synthesis of CuO towards commercialization.

Here we present results on the structure and properties of copper oxide nanostructured films deposited by successive ionic layer adsorption and reaction (SILAR) on indium tin oxide (ITO) substrates. SILAR is a simple chemical method used for the synthesis of large area metal oxides in which thin films are obtained by immersing a substrate into separately placed cationic and anionic precursor solutions [43]. The deposition rate, thickness, particle size and morphology of the film can be easily controlled by changing the deposition cycle, temperature, pH and solvent concentration. Any substrate, regardless of material type (be it plastic, glass, metal etc.) can be used for SILAR deposition. Likewise any substrate shape (be it circular, rectangular, dimensionless etc.) can be used. In addition to these, the surface profile (rough, smooth etc.) of the substrate does not restrict its use for SILAR. We show that CuO nanostructured films obtained by few deposition cycles (as low as 10 cycles) at very short deposition times gave an enhanced specific capacitance of 566.33 Fg^{-1} with good electrochemical cycling stability (100% coulombic efficiency after 1000 cycles). This is in comparison to previous results in the literature [27,34,37,44].

2. Experimental

All chemicals were of analytical grade and were used without further purification. CuO nanostructured films were deposited on ITO using the SILAR approach. Prior to deposition, the ITO substrates were cleaned with detergent, rinsed with water and ultrasonicated in a mixture of water and acetone for 10 min. The cationic precursor used is 0.1 M cuprous acetate ($CH_3COO)_2Cu.H_2O$) made alkaline (pH ~ 10.5) with ammonium hydroxide (NH_3OH) and maintained at room temperature. The anionic precursor used was distilled water with 1% H_2O_2 (source of the OH$^-$) maintained at a temperature of 60–70 °C. A complete SILAR cycle involves the alternate immersion of the ITO substrate vertically into the alkaline Cu salt bath (source of Cu$^+$) for 20s, the 1% H_2O_2 for 20s and rinsing in distilled kept at room temperature for another 20s. This cycle was repeated 10–40 times and at the end of the complete cycle, the nanostructured films were rinsed thoroughly with distilled water and annealed in air at 300 °C for 1 h to convert the hydroxide phase to oxide. The mass of the deposited film was determined using a four-digit weighing balance (Mettler Toledo) and applying the weight difference method. X-ray Photoelectron Spectroscopy (XPS) was used to determine the electronic and chemical composition of the deposited films. The surface morphology of CuO thin films was characterized by Scanning electron microscopy (SEM) and images were recorded using a Carl Zeiss Ma-10 field emission electron microscope operating at 20 keV and by atomic force microscopy (AFM) (Smart SPM 1000- AIST-NT Inc.) in tapping mode. The pore distribution was extracted from AFM images using the Gwyddion (threshold method) software.

Raman spectroscopy was performed with a confocal optical microscope (Omegascope AIST-NT Inc.) coupled with a Raman spectrometer from Tokyo Instruments (Nanofinder-30). The light source is a continuous wave diode-pumped solid-state (CW-DPSS) laser with a wavelength of 532 nm (Cobolt Inc.). The laser was focused onto the sample with a 100X objective (N.A 0.7) and a power of 10 mW. The Raman signal was dispersed into the spectrometer with a grating of 1800 lines/mm, then, a charge-coupled detector (CCD) (iDus 401, Andor Inc.) was used to collect the Raman spectra. X-ray diffraction (XRD) measurements were performed using an XPERT PRO diffractometer. The electrochemical properties of the films were determined using a potentiostat (Princeton Applied Research VersaSTAT) in a three-electrode system, which consists of the working electrode (deposited films on ITO), a large-sized graphite counter electrode and a KCl-saturated Ag/AgCl reference electrode. The electrolyte used in all studies was 0.5 M Na_2SO_4. EIS was performed using a three electrode system in 0.5 M $NaSO_4$ electrolyte and at a freqency range of 10 mHz–100 kHz with scanning in AC mode with a constant voltage amplitude of 10 mV.

3. Results and discussion

3.1. Nanostructured film formation

Addition of aqueous ammonia (NH_4OH) to the ($CH_3COO)_2Cu.H_2O$ solution causes the ionic product to become greater than the solubility product [45], and $Cu(OH)_2$ is precipitated causing the solution to become turbid. Complex copper $[Cu(H_2O)_2(NH_3)_4]^{2+}$ ions are formed on addition of excess ammonia due to ligand exchange reactions. These ions prevent further precipitation and make the solution clear and transparent. This can be explained by equation 1 [27]:

$$Cu(H_2O)_4(OH)_2 + 4NH_3 \rightarrow [Cu(NH_3)_4(H_2O)_2]^{2+} + 2H_2O + 2OH^- \qquad (1)$$
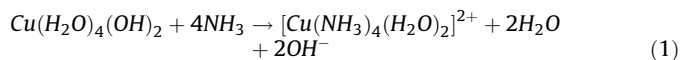
Film deposition involves the ion-by-ion growth of the Cu^{2+} at nucleation sites on the surface of the immersed ITO. Immersion of the ITO into the complex copper salt bath causes Cu^+ to stick to the walls of the substrate due to attractive force between the ions and the substrate. Upon immersion of the ITO with the adsorbed Cu^{2+} into the 1% H_2O_2 solution, OH^- species are attracted to the substrates from the solution to form copper hydroxide on the ITO. Additional alternate immersion into the solutions causes further growth at the nucleation sites, which eventually forms a film on the substrate. The hydroxide may be converted into oxide by annealing at 300 °C in air for 1 hr.

Film thickness was determined by using the gravimetric weight difference method, using the relation [46]:

$$\tau = \frac{m}{A\rho_b} \qquad (2)$$

where τ is the thickness of the film, m is the mass of the deposited film, A is the area of the film, and ρ_b is the bulk density of the CuO (0.79 gcm^{-3}). Thicknesses of 25 and 182 μm were obtained for 10 and 40 cycles of the CuO nanostructured films respectively. This implies that the thickness increases with the number of cycles, as expected.

3.2. X-ray Photoelectron Spectroscopy (XPS)

Fig. 1a displays the electronic and chemical composition of the deposited films as determined from X-ray Photoelectron Spectroscopy (XPS). The spectra identify the presence of carbon, oxygen and copper. The peak of non-oxygenated carbon (C 1s) is detected at a binding energy (BE) of about 285.0 eV (Fig. 1b). The XPS spectrum of the Cu 2p core level of the CuO is shown in Fig. 1c. The oxidation state of copper is confirmed from the splitting of the Cu 2p peak.

The presence of peaks of Cu $2p_{3/2}$ and Cu $2p_{1/2}$ at BE of 933.95 and 953.75 eV respectively suggests the presence of Cu^{2+} on the sample. The observation of satellite peaks at BE of 943.95 and 962.55 eV on the high energy side of each of Cu $2p_{3/2}$ and Cu $2p_{1/2}$ respectively, confirms the presence of Cu^{2+} on the sample due to the existence of the unfilled Cu^3d^9 shell [37]. The binding energy difference between Cu $2p_{1/2}$ and Cu $2p_{3/2}$ peaks (around 19.8 eV) confirms the presence of the CuO phase in the sample [47]. The O 1s spectra for the nanostructuerd CuO (Fig. 2d) exhibit a strong peak with a shoulder peak at a higher binding energy. The peak at BE around 529.7 eV is most likely due to lattice O^{2-} while the shoulder peak around BE of 531.3 eV may be attributed to surface oxygen species such as adsorbed oxygen O^- [48,49].

3.3. XRD analysis

The structural properties of the deposited films were further investigated using XRD in the 2θ range of 10–80. Fig. 2 shows the XRD pattern of CuO deposited on ITO. Strong peaks corresponding to the (111) and (200) direction planes of CuO are observed. Other identifiable peaks of CuO are at angles (2θ) values of 48.7°, 62.3°, and 68° corresponding to the diffraction planes (202), (-311) and (220) respectively (JCPDS #. 80–0076). The films exhibit very sharp peaks, which is most likely the result of the enhanced crystallinity of the films.

3.4. Energy Dispersive X-ray spectroscopy (EDS)

The EDS spectrum of the nanostructured CuO film with the associated percentage weight and atomic percent of the elemental composition of the film is shown in the inset of Fig. 3(b and d) respectively. The spectrum for the copper oxide nanostructured
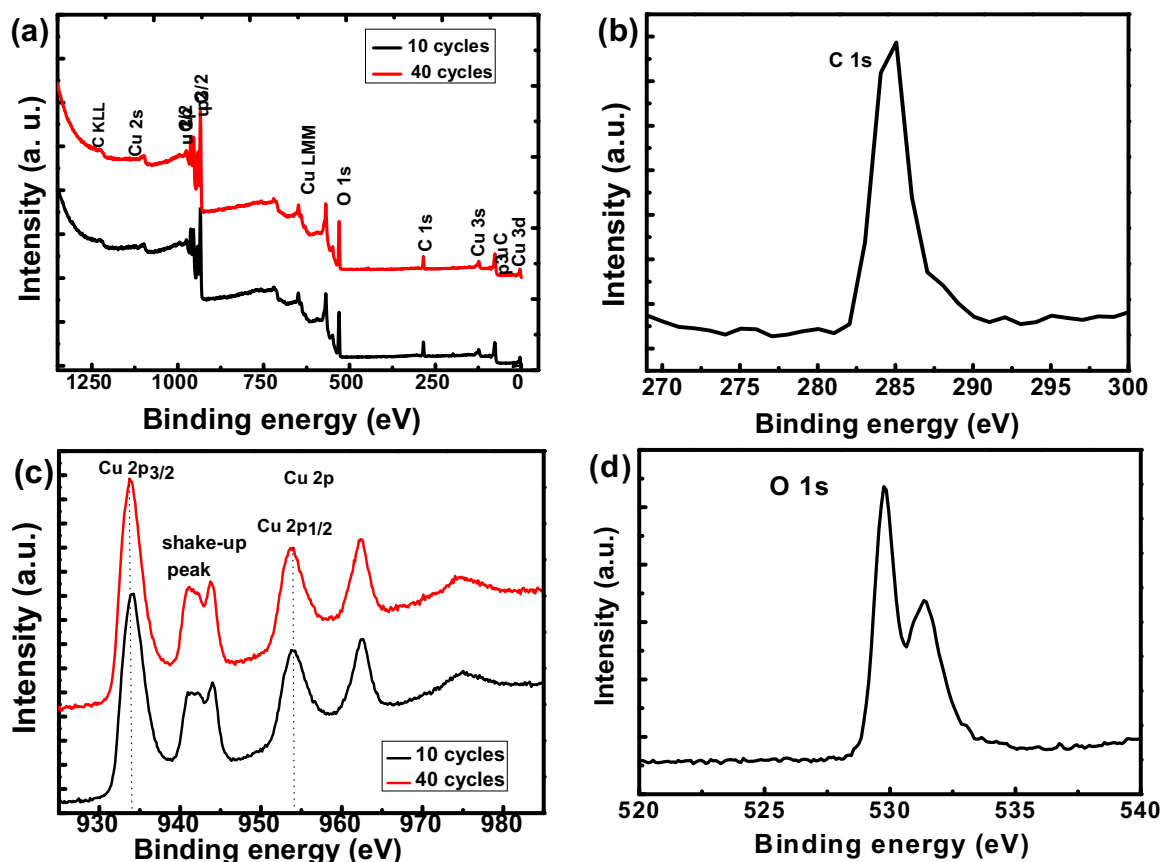

Fig. 1. (a) Full XPS of the CuO films (b) core level XPS of C 1s (c) core level XPS spectra of Cu 2p (d) O 1s spectrum of the CuO film.
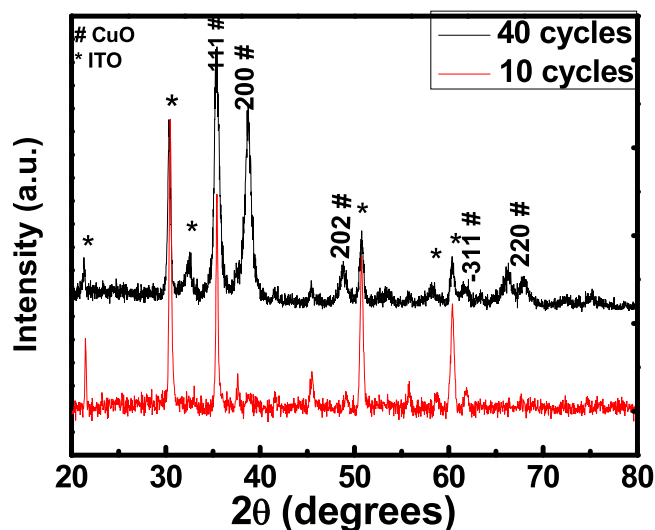
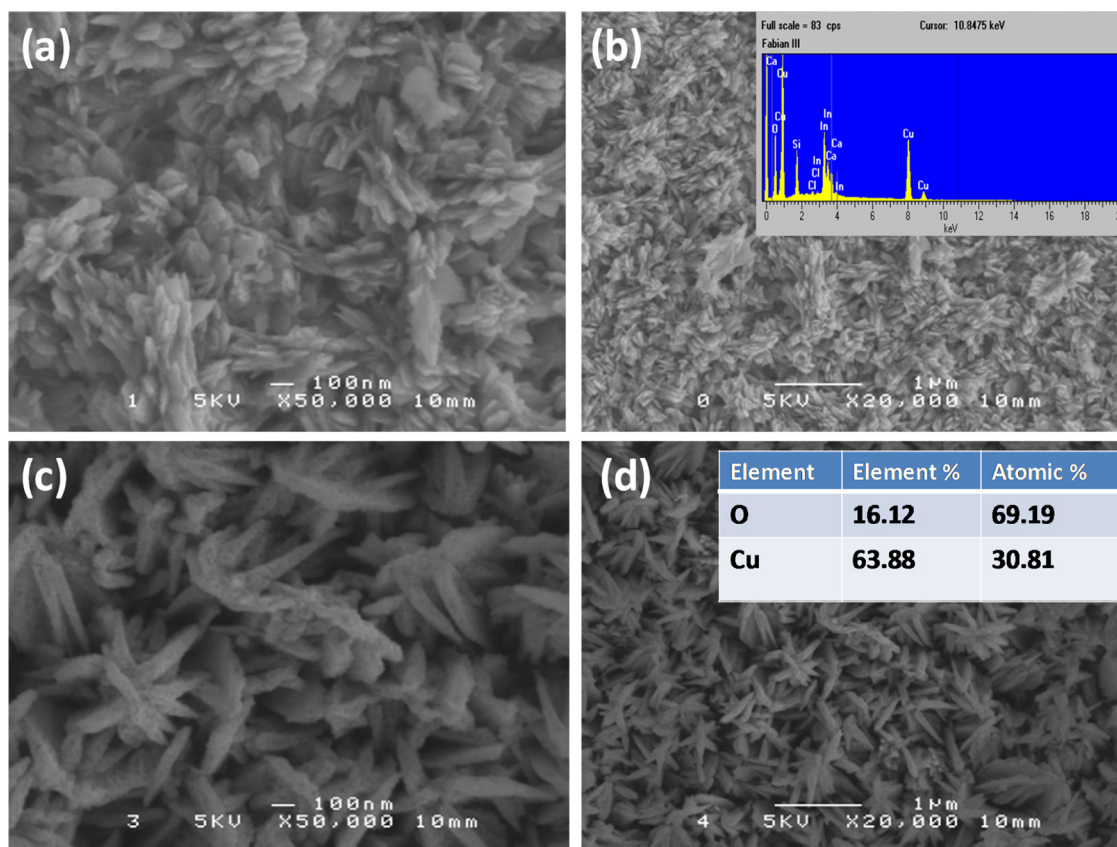**Fig. 2.** XRD pattern of the CuO films on indium doped tin oxide (ITO).

Fig. 3. SEM images of the deposited films (a and b) 10 cycles and (c and d) 40 cycles at two different magnifications 50 K and 20 K (Inset b) EDS spectrum of the CuO films showing the peaks of Cu and O at the appropriate energy levels (Inset d) Table showing Elemental Composition of CuO determined from EDS.

film shows strong peaks of Cu and O at the appropriate energy levels. Other elements (In, Si, Mg, Al) emanate from the ITO substrate used.

3.5. Surface morphology by SEM

The surface morphology of the films as imaged by SEM is shown in Fig. 3(a-d) for 10 and 40 cycles at two different magnifications. The micrographs indicate that the coverage of

the films extends across the entire substrates. The 10-cycle film showed the formation of porous nanosheets of irregular shapes and sizes spread all over the surface while the 40-cycle film showed a porous outgrowth of nanorod-like grains of uneven sizes from the nucleation centres. The microstructure formation process of the films starts with nucleation (heterogeneous reaction at the surface), grain aggregation and subsequent self-organization of the films into larger particles. The grains grow from the nucleation centre to form nanosheets
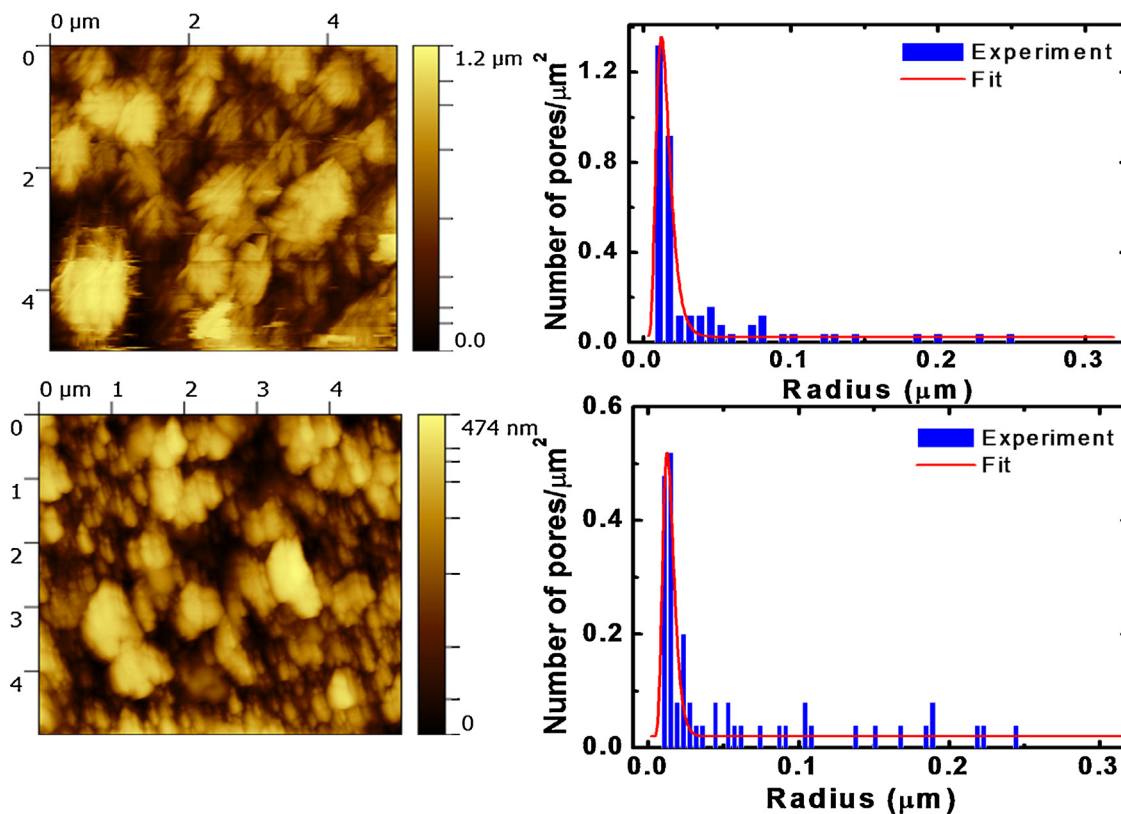
for the 10- cycle film while further cycles lead to the formation of nanorods. The porosity of the films makes them a good material for electrolyte penetration to aid intercalation/deintercalation of ions.

3.6. Surface morphology by AFM

The surface morphology of CuO films was characterized by AFM (Smart SPM 1000- AIST-NT Inc.) in tapping mode. In Fig. 4, we plot surface morphologies of the films imaged by AFM (left panels) and the number of pores per unit area (μm^2) as a function of pore radius (right panels) for the 10 and 40 cycle films. The average size of the grains was estimated from AFM topographies, by using the height-height correlation function (HHCF), the typical values are 47 ± 2.4 nm for 10 cycles and 35 ± 2.9 nm for 40 cycles, while the extraction of the average size of the pores with its deviation were estimated using the lognormal distribution function that fit well with the pore distribution in the samples.

In the AFM images of Fig. 4 (a-b), in the 10 cycle case, we observed small nanosheets with different size oriented in different directions, with some small links between them, while in the case of 40 cycles we identified small nanorods. From the pore size distribution in Fig. 4 (c-d), we observed twice the number of pores in the 10 cycles than 40 cycles. The transformation of the nanosheets (10 cycles with more pores) to nanorods (40 cycles with less pores) led to a decrease in the number of pores, hence reducing the accessibility or permeability of the electrolytes as observed during the electrochemical process. The observations from AFM images are in good agreement with SEM observations.

3.7. Raman spectroscopy

CuO is a semiconductor material with a monoclinic crystal structure attributed to a space group symmetry of C_6^{2h}. In this study, Raman spectroscopy was performed to obtain additional information on the crystal structure of CuO nanostructures. The primitive cell contains two molecular units, and thus the Brillouin zone center can include twelve vibrational modes: three acoustic modes ($A_u + 2B_u$), six infrared active modes ($3A_u + 3B_u$) and three Raman active modes ($A_g + 2B_g$). These normal lattice vibrations at the Γ point of the Brillouin zone are determined on the basis of group theory by the equation [49]:
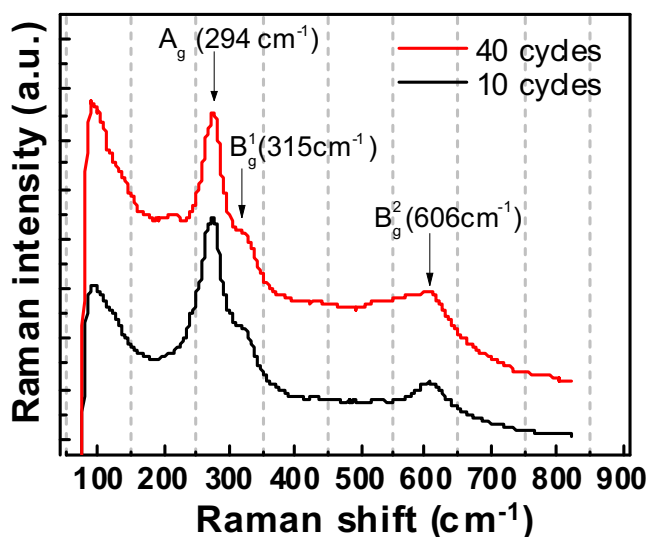
$$\Gamma = 4A_u + 5B_u + A_g + 2B_g \tag{3}$$

Fig. 5 shows three Raman peaks of CuO respectively at 294 cm^{-1}, 315 cm^{-1} and 606 cm^{-1}. The peak at 294 cm^{-1} is attributed to the A_g mode while the two latter peaks at 315 and 606 cm^{-1} are assigned respectively to B_g^1 and B_g^2 modes of CuO [50,51]. In accordance with XRD results, we also observe that the Raman peak of the 10- cycle CuO is broader than the 40-cycle, this can be attributed to the effect of small crystallite sizes of the 10-cycle CuO nanosheets. In addition, the intensity of Raman peaks changes between the two types of nanostructures, which implies that the lattice symmetry is affected by sample defects [52].

3.8. Electrochemical characterization

3.8.1. Cyclic Voltammetry (CV)

We used cyclic voltammetry to determine the accessibility of the electrode material to the electrolyte and hence the capacitive behavior. The CV curves of the films on ITO glass substrates

Fig. 4. AFM images of the deposited films of CuO (a and b) 10 cycles and 40 cycles respectively at scan area 5 μm × 5 μm (c and d) Number of pores per μm^2 as a function of pore radius (blue column), best Fit with lognormal function (red curve) 10 cycles and 40 cycles respectively. It is fitted with a Lognormal distribution function: $f(x) = f_{max}(\mu)$*exp$((-1/(2*\sigma^2))*(\ln(x/\mu))^2)$ where σ=0.37 nm (standard deviation) and μ=12 nm (average size of pore) for 10 cycles and σ (standard deviation)= 0.28, and μ=12.5 nm for 40 cycles.

Fig. 5. Room-temperature Raman spectra of CuO obtained after two different deposition- cycles, 40 cycles (red color) and 10 cycles (black color). (For interpretation of the references to color in this figure legend, the reader is referred to the web version of this article.)

recorded in 0.5 M NaSO$_4$ aqueous solution at various scan rates is shown in Fig. 6(a and b). CV curves of the CuO nanostructured films exhibit very sharp redox peaks indicating that the electrochemical capacitance is due mainly to redox reactions rather than EDLC. The potential windows for the 10- and 40-cycle differ slightly because of the differences between their voltammetric evolutions; the 10-cycle film showed no activities in the negative potential, thus the need to start the CV at 0 V, while the case is different for the 40-cycle film that showed redox-activity up to −0.2 V. The redox peaks corresponds to the reduction of Cu^{2+} to Cu$^+$ and the oxidation of Cu$^+$ to Cu^{2+} during the intercalation/deintercalation of smaller H$^+$ or the bigger Na$^+$ into the matrix of the material. It has been shown that the redox activity of CuO during cyclic voltammetry is dependent on the pH of the electrolyte used [34,53]. In a neutral electrolyte such as the one we used here, two mechanisms are proposed. One is the intercalation and de-intercalation of the ions (H$^+$ and Na$^+$) into the matrix while the other is the adsorption of the ions on the surface rather the bulk of the material. Equations (4) and (5) [27,36] are used to represent both processes, as follows:

$$2CuO + 2A^+ + 2e^- \Leftrightarrow Cu_2OOA \qquad (4)$$

$$(2CuO)_{surface} + 2A^+ + 2e^- \Leftrightarrow (Cu_2OOA)_{surface} \qquad (5)$$
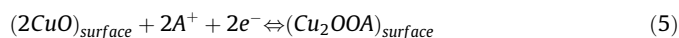
The current density increased with the scan rate as shown in the CV curves. This implies that the redox processes is mainly governed by the insertion and de-insertion of the ions (H$^+$ and Na$^+$) in the CuO electrodes. The CV of the bare ITO substrate is shown in the inset of Fig. 6a for comparison and it indicates a very low current density of up to 10^3 less than that the substrates with the CuO films. To ensure that the ITO does not contribute to the redox activity, the CV of the bare ITO and that of the 40- cycle film at 10 mVs^{-1} is compared as shown in the inset of Fig. 6b. It is obvious that the ITO contributes little or nothing to the redox process.

The specific and volumetric capacitances were calculated from the CV curves using equations 6 and 7 as follows: [27,30,54,55]

$$C_s = \frac{\int Idt}{m(^dV/_dt)} \qquad (6)$$

$$C_v = \frac{\int Idt}{A.\tau(^dV/_dt)} \qquad (7)$$

where C_s and C_v are the specific and volumetric capacitance in Fg^{-1}, Fcm^{-3} respectively, $\int Idt$ is the area under the CV curve, m is the mass of the deposited in g (obtained by measuring the weight difference of the substrates before and after deposition), dV/dt is the scan rate in mVs^{-1}, A is the area of the electrode in cm^2 and τ is the thickness in cm. The graph of the calculated specific (gravimetric) and volumetric capacitance for the films as a function of the scan rates are shown in Fig. 6c. The specific capacitance generally decreases with increasing scan rates. The decrease in the specific capacitance at higher scan rates implies that not all the parts of the electrode surface are used at higher scan rates. The specific capacitance calculated using equation 6 at a scan rate of 5 mVs^{-1} is 566.33 and 211. 87 Fg^{-1} for the 10- and 40-cycle CuO nanostructured films respectively. The 10-cycle film gave a remarkably higher specific capacitance (566.33 Fg^{-1}) than the 40-cycle film (211.87 Fg^{-1}). This occurs as a result of the availability of more pores and smaller thickness present in the 10-cycle film than the 40-cycle film. Enhanced porosity allows for more electrolyte penetration and hence increases charge storage. The higher thickness of the 40-cycle film as a result of increase in mass loading also contributed to the lower C_g since only the surface/near surface layer of the CuO that is close to the current collector substrate is electrochemically active. The values of the specific capacitance for the 10-cycle CuO film are higher but comparable to the highest value (535 Fg^{-1}) obtained by Gund et al., [42] for surfactant assisted CuO films but much higher than the highest values (396 Fg^{-1}, 43 Fg^{-1}) obtained by Dubal et al., [37,54] and 37 Fg^{-1} by Patake et al. [56]. This comparative analysis shows that our surfactant-free 10–cycle CuO nanostructured films are very good potential electrodes for pseudocapacitor applications.

3.8.2. Galvanostatic Charge discharge (GCD)

Galvanostatic charge-discharge (GCD) measurements were carried out in the same electrolyte condition as the CV. It is well-established that GCD is the most accurate method to determine the supercapacitive behaviour of electrochemical
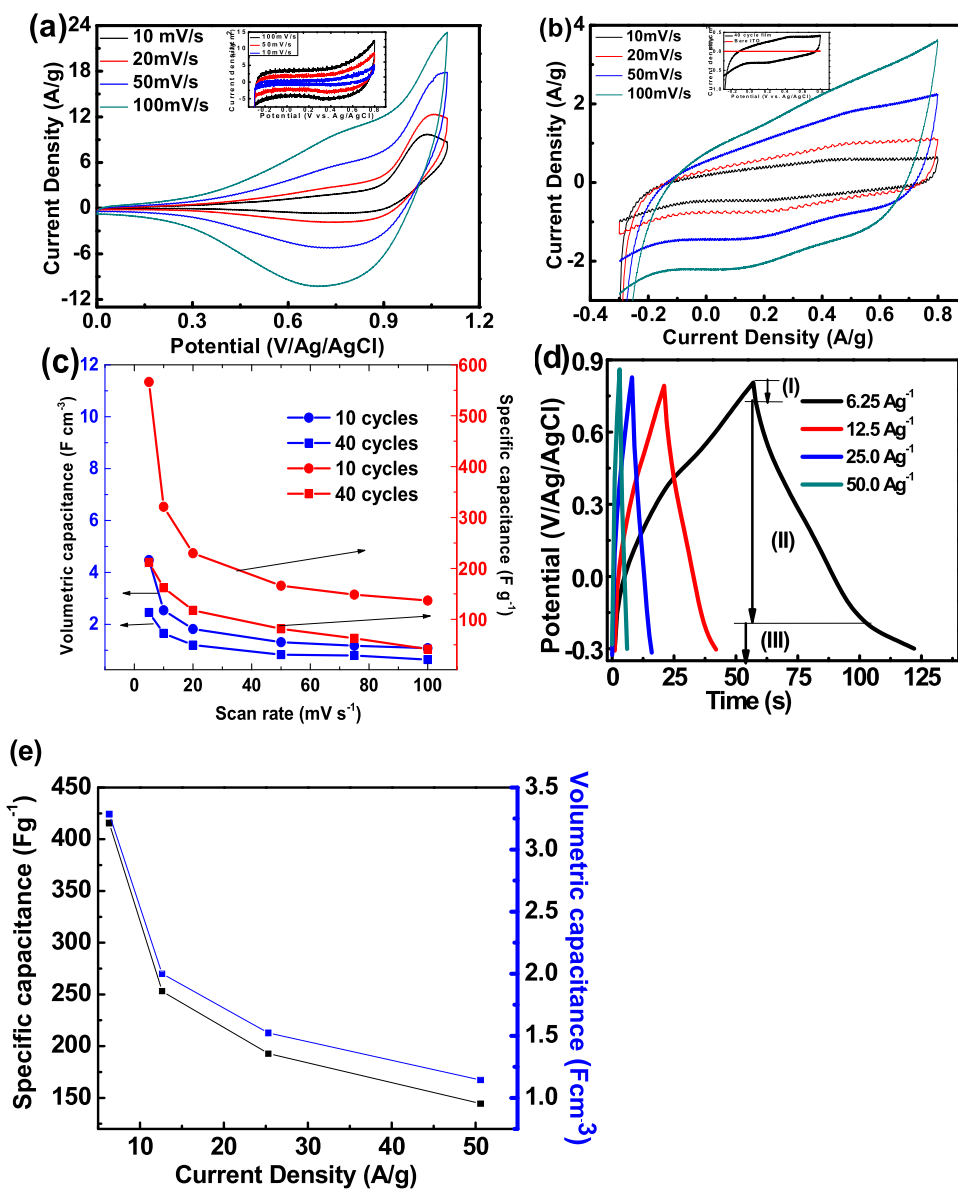
Fig. 6. Cyclic voltammetry curves of the electrode films (a) 10 cycles (inset: CV of the bare ITO substrate) (b) 40 cycles (inset: CV of the bare ITO and 40–cycle film at 10 mVs^{-1}) (c) Specific capacitance vs. scan rate for CuO films. (d) Galvanostatic charge-discharge curve for the 10-cycle film at various current densities (e) The plot of specific and volumetric capacitance at various current densities for the 10-cycle CuO film.

capacitors compared to CV or EIS [57]. GCD of the 10-cycle electrode films is displayed in Fig. 6d. Interestingly, the GCD curves could only be obtained at high current densities (6.25–50 A g^{-1}) as every effort we made to go below 6.25 A g^{-1} was unsuccessful. This behavior is a clear indication that our experimental conditions generate CuO film of high power density. The GCD curves of the copper oxide showed three variation ranges. The first is the sudden

drop in current at the onset of discharge, (region I) which is due to internal resistance. The second (region II) is the linear variation of the time dependence of the potential, which is a characteristic of double layer capacitance while the third (region III) is the slope dependence of the potential, which is due to redox reactions resulting in pseudo-capacitance at the electrode/electrolyte interface [26]. The specific capacitance was calculated from the

Table 1
Comparison of the pseudocapacitive performance of CuO films compared with other 3-electrode systems in the literature.

Aqueous Electrolyte	Morphology	C_s/F g^{-1}	E_s/Wh kg^{-1}	P_{max}/kW kg^{-1}	Ref.
0.5 M Na$_2$SO$_4$	Nanosheets	415	127.3	6.64	This work
1 M Na$_2$SO$_4$	Nanosheet clusters	413	46	0.70	[27]
1 M Na$_2$SO$_4$	Micro-woolen-like	340	39	0.50	[36]
1 M Na$_2$SO$_4$	Nanobuds	–	44	1.00	[37]
1 M Na$_2$SO$_4$	Yarn ball-like	436	–	–	[42]
1 M Na$_2$SO$_4$	Cauliflower like	162	22	0.60	[63]

GCD using equation 8:

$$C_s = \frac{I \times t_d}{\Delta V \times m} \qquad (8)$$

where C_s is the specific capacitance, I is the charge/discharge current, t_d is the discharge time, ΔV is potential window and m is the mass of the active material within the film.

The values of the specific capacitance as obtained from the GCD as a function of current density is shown in Fig. 6e. The C_s decreases with increase in the current density and the highest value of 415 Fg^{-1} is obtained at a current density of about 6.25 Ag^{-1}. The calculated C_s from the GCD curve are shown in Table 1 and is compared with other works on CuO in a three electrode configuration. Generally, in comparison with other works as shown in Table 1, our electrode offered a relatively higher electrochemical super capacitive performance especially with respect to power density.

The long-term stability of the film was investigated by potential cycling at a current density of 50 Ag^{-1} and the capacitance retention after 1000 cycles is shown in Fig. 7a. The capacity retention of the CuO film is found to be 100% after 1000 cycles. The GCD curve of the oxide film showing the 1st and the 1000th cycle is shown in Fig. 7b and 7c, respectively. The figures indicate that the electrode is very stable and itable and is a very good material for supercapacitive applications.

Energy density and power density are used to compare energy content and rate capabilities respectively for energy storage devices. The relationship between these two parameters is demonstrated by using the Ragone plot, which gives a comparison for various energy devices. The specific energy (SE) specific power and the columbic efficiency (η %) were calculated using the following equations [55,58]:

$$SE = \frac{I \times t_d \times \Delta V}{m} \qquad (9)$$

$$SP = \frac{I \times \Delta V}{m} \qquad (10)$$

$$Coulombic\ efficiency(\eta\%) = \frac{t_d}{t_c} \times 100 \qquad (11)$$

where t_c is the charging time. The maximum specific energy and specific power obtained for CuO are 127.29 Whkg^{-1} and 53.13 kWkg^{-1} at current densities of 6.25 Ag^{-1} and 50 Ag^{-1}, respectively. The coulombic efficiency obtained for the copper oxide for the 1st and 1000th cycle is 100% which implies that there is no loss in the redox processes even after 1000 cycles. This demonstrates the high stability of the CuO film.

The Ragone plot for the copper oxide film is shown in Fig. 7d. The specific energy decreased from 127.29 to 44.27 Whkg^{-1} while the specific power increased from 6.64 to 53.13 kWkg^{-1} with increased current density of 6.25 Ag^{-1} to 50 Ag^{-1}. The decrease in the specific energy suggests that parts of the electrode's surface are not accessible at high charging-discharging current. The increasing trend of the specific power indicates that the discharging capacity of the pseudocapacitor is directly proportional to the discharge current. The values we obtained for power density are greater than most carbon-based materials and their composites [59–62].

3.8.3. Electrochemical Impedance spectroscopy (EIS)

The Nyquist plot for CuO is shown in Fig. 8a. Using the ZsimpWinsoftware, the Nyquist plot was satisfacorily fitted with the Voigt electrical equivalent circuit (see inset, Fig. 8a) which comprises the R_s (electrolyte resistance), R_{ct} charge tranfer resistance overthe interface between the electrode and the electrolyte, and constant phase element (CPE or Q) due to inhomogeneity at the electrode/electrolyte surface and dynamic disorder associated with diffusion [64]. From the fitted circuit, R_s was 37.82 ± 0.57 Ω, R_{ct1} and R_{ct2} were 38.18 ± 3.4 and 214 ± 8.53 Ω, respectively; Q_1 and Q_2 were 5.44 ± 1.31 and 3.32 ± 0.97 mF.s(α-1), respectively; while n_1 and n_2 were 0.85 ± 0.2 and 0.63 ± 0.17,
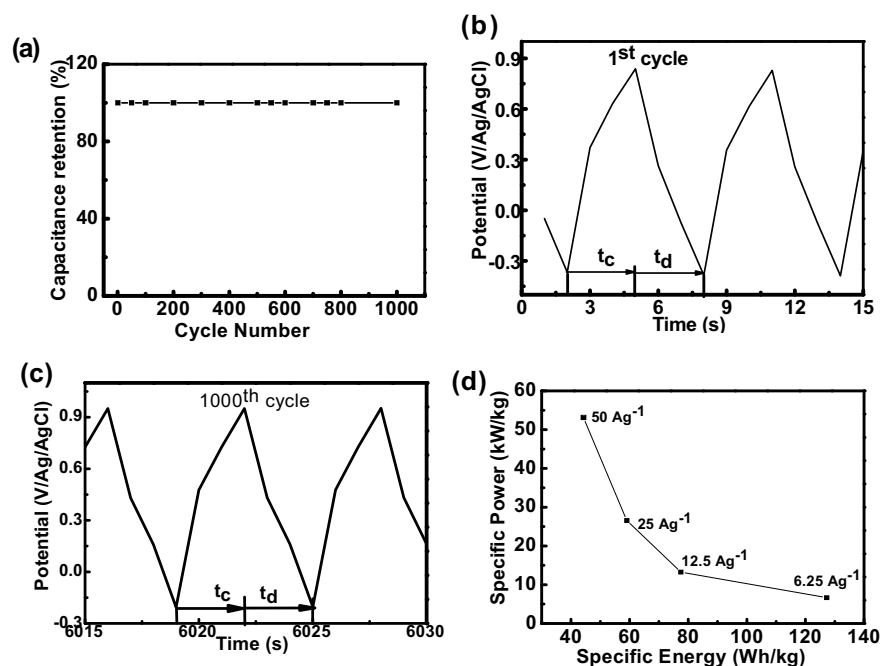

Fig. 7. (a) Variation of capacity retention of the electrode films with number of cycles (b) GCD of the CuO indicating the 1st cycle (c) GCD of the CuO indicating the 1000th cycle (d) the Ragone plot of the CuO nanostructured film electrode.
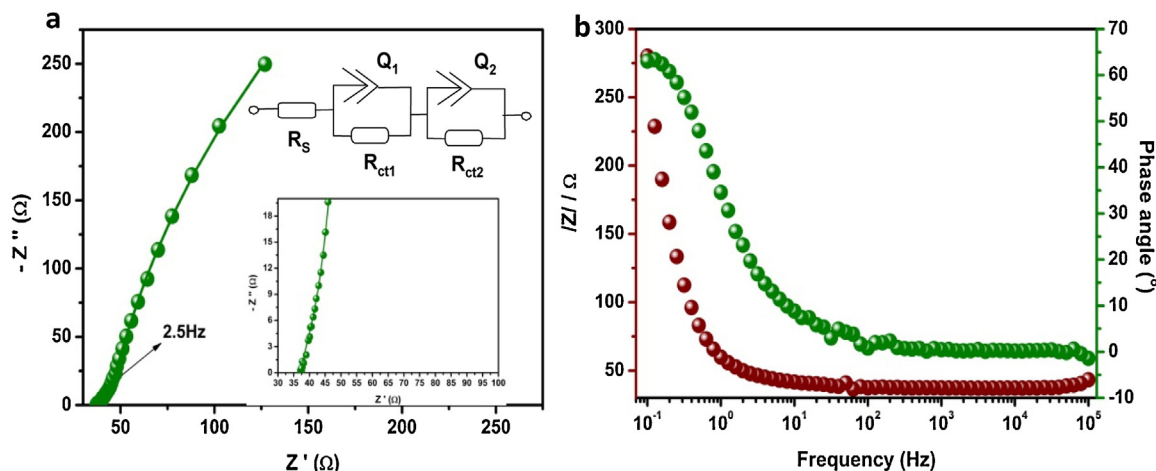
Fig. 8. (a) Nyquist plot (inset equivalent circuit) (b) Bode plot for the CuO film electrode.

respectively. The impedance of the CPE is defined as shown in equation 12, as follows [65]:

$$Z_{CPE} = \frac{1}{Q(jw)^n} \qquad (12)$$

where Q is the frequency-independent constant relating to the surface electroactive properties, w represents the radial frequency. For $n = 0$, the CPE is a pure resistor; $n = 1$, CPE is a pure capacitor, $n = -1$, CPE is an inductor; while $n = 0.5$ it is Warburg impedance (Z_w). The n value observed in our work is greater than 0.5 but less than the ideal value of unity for pure EDLC, which confirms that the electrode material behaves like a pseudocapacitor.

The Bode plot is shown in Fig. 8b. The magnitude of impedance/ Z/increases with frequency in the high frequency region but is frequency independent in the low frequency region. This frequency independent region is where the impedance is purely resistive and the value on the log/Z/axis gives the solution resistance. The phase angle indicates similar dependence on frequency as the/Z/. The phase angle of about 62.5° also indicates the pseudocapacitive nature of the electrode. The knee frequency ($f_o, \varphi = 45°$) is a measure of the power capability of a supercapacitor; the higher the f_o the more rapidly the supercapacitor can be charged and discharged (an ideal supercapacitor has a charge/discharge time of $1 \sim 30$ sec.). In addition to this, the higher the f_o, the higher the power density that can be achieved from the supercapacitor. From Fig. 8, the value of f_o was calculated as $ca. 2.5$ Hz (time constant ≈ 0.4 s), which further corroborates the higher power performance of the nanostructured CuO thin film electrode.

4. Conclusions and perspectives

A simple, cost effective, additive free and binderless chemical method was used to deposit nanostructures of CuO films on ITO. The nanosheet and nanorodlike films showed good porosity for application as supercapacitive electrodes. A high specific capacitance of up to 566.33 Fg^{-1} is obtained for the film deposited after 10 cycles. This value is higher than most of the previously obtained results and is attributed to the porous nanostructure of the electrode. This morphology permits easy contact and penetration of the electrolyte for longer electron pathways. In addition, the electrode showed no sign of depreciation even after 1000 cycles giving a columbic efficiency of 100% after the 1000th cycle, indicating that our chemically synthesized CuO film electrodes have excellent properties for use as supercapacitor electrode. Based on these encouraging results, future research efforts will be geared towards investigating the electrochemical properties of the

tandem structure of active materials (e.g. CuO films) working under extreme conditions such as high temperature and high pressure.

References

[1] Y. Daniel, The Quest: Energy, Security, and the Remaking of the Modern World, Penguin press, 2012, pp. 150.

[2] M. Chaker, F. Rosei, Materials research in Africa: Rising from the Falls, Nature Materials 11 (2012) 187–188.

[3] F. Rosei, L. Vayssieres, P. Mensah, Materials in the Developing World: Challenges and Perspective for Africa, Advanced Materials 20 (2008) 4627–4640.

[4] A. Vlad, N. Singh, J. Rolland, S. Melinte, P.M. Ajayan, J.F. Gohy, Hybrid supercapacitor-battery materials for fast electrochemical charge storage, Scientific Reports 4 (2014) 4315.

[5] G. Wee, W.F. Mak, N. Phonthammachai, A. Kiebele, M.V. Reddy, B.V.R. Chowdari, G. Gruner, M. Srinivasan, S.G. Mhaisalkar, Particle Size Effect of Silver Nanoparticles Decorated Single Walled Carbon Nanotube Electrode for Supercapacitors, J. Electrochemical Society 157 (2010) A179–A184.

[6] F. Rosei, Nanostructured surfaces: challenges and frontiers in nanotechnology, J. Phys.: Cond. Matt. 16 (2004) S1373–S1436.

[7] T.-M. Wu, S.-H. Lin, Characterization and electrical properties of polypyrrole/ multiwalled carbon nanotube composites synthesized by in situ chemical oxidative polymerization, J. Polymer Science: Part B: Polymer Physics 44 (2006) 1413–1418.

[8] G.S. Gund, D.P. Dubal, S.B. Jambure, S.S. Shinde, C.D. Lokhande, Temperature influence on morphological progress of Ni(OH)$_2$ thin films and its subsequent effect on electrochemical supercapacitive properties, J. Materials Chemistry A 1 (2013) 4793–4803.

[9] D.P. Dubal, C.D. Lokhande, Significant improvement in the electrochemical performances of nano-nest like amorphous MnO$_2$ electrodes due to Fe doping, Ceramics International 39 (2013) 415–423.

[10] A.C. Nwanya, C.J. Jafta, P.M. Ejikeme, P.E. Ugwuoke, M.V. Reddy, R.U. Osuji, K.I. Ozoemena, F.I. Ezema, Electrochromic and electrochemical capacitive properties of tungsten oxide and its polyaniline nanocomposite films obtained by chemical bath deposition method, Electrochimica Acta 128 (2014) 218–225.

[11] C. Bora, S.K. Dolui, Fabrication of polypyrrole/graphene oxide nanocomposites by liquid/liquid interfacial polymerization and evaluation of their optical, electrical and electrochemical properties, Polymer 53 (2012) 923–932.

[12] Q. Cheng, J. Tang, J. Ma, H. Zhang, N. Shiny, L. Quin, Graphene and nanostructured MnO$_2$ composite electrodes for supercapacitors, Carbon 49 (2011) 2917–2925.

[13] D.-W. Wang, F. Li, M. Liu, H.-M. Cheng, Improved capacitance of SBA-15 templated mesoporous carbons after modification with nitric acid oxidation, New Carbon Materials 22 (2007) 307–314.

[14] M. Kaempgen, C.K. Chan, J. Ma, Y. Cui, G. Gruner, Printable Thin Film Supercapacitors Using Single-Walled Carbon Nanotubes, Nano Letters 9 (2009) 1872–1876.

[15] N.H. Basri, M. Deraman, S. Kanwal, I.A. Talib, J.G. Manjunatha, A.A. Aziz, R. Farma, Biomass and Bioenergy, Supercapacitors using binderless composite monolith electrodes from carbon nanotubes and pre-carbonized biomass residues, Biomass and Bioenergy 59 (2013) 370–379.

[16] A.S. Adekunle, K.I. Ozoemena, Electrosynthesised Metal (Ni, Fe, Co) Oxide Films on Single-Walled Carbon Nanotube Platforms and Their Supercapacitance in Acidic and Neutral pH Media, Electroanalysis 23 (2011) 971–979.

[17] A.T. Chidembo, K.I. Ozoemena, Electrochemical Capacitive Behaviour of Multiwalled Carbon Nanotubes Modified with Electropolymeric Films of Nickel Tetraaminophthalocyanine, Electroanalysis 22 (2010) 2529–2535.

[18] X. Yu, B. Lu, Z. Xu, Super Long-Life Supercapacitors Based on the Construction of Nanohoneycomb-Like Strongly Coupled CoMoO4-3D Graphene Hybrid Electrodes, Adv. Mater 26 (2014) 1044–1051.

[19] Z. Tang, C.-H. Tang, H. Gong, A high Density Asymmetric Supercapacitor from Nano- architectured $(NiOH)_2^-$/carbon Nanotube Electrodes, Adv. Funct. Mater. 22 (2012) 1272–1278.

[20] G.P. Wang, L. Zhang, J.J. Zhang, A Review of Electrode Materials for Electrochemical Supercapacitors, Chemical Society Reviews 41 (2012) 797–828.

[21] R. Farma, M. Deraman, A. Awitdrus, I.A. Talib, E. Taer, N.H. Basri, J.G. Manjunatha, M.M. Ishak, B.N.M. Dollah, S.A. Hashmi, Preparation of highly porous binderless activated carbon electrodes from fibres of oil palm empty fruit bunches for application in supercapacitors, Bioresource Technology 132 (2013) 254–261.

[22] P.R. Deshmukh, S.N. Pusawale, R.N. Bulakhe, C.D. Lokhande, Supercapacitive performance of hydrous ruthenium oxide ($RuO_2 \cdot nH_2O$) thin films synthesized by chemical route at low temperature, Bulletin of Material Science 36 (2013) 1171–1176.

[23] A.D. Jagadale, V.S. Kumbhar, R.N. Bulakhe, C.D. Lokhande, Influence of electrodeposition modes on the supercapacitive performance of Co_3O_4 electrodes, Energy 64 (2014) 234–241.

[24] A.D. Jagadale, D.P. Dubal, C.D. Lokhande, Electrochemical behavior of potentiodynamically deposited cobalt oxyhydroxide (CoOOH) thin films for supercapacitor application, Materials Research Bulletin 47 (2012) 672–676.

[25] D.P. Dubal, A.D. Jagadale, C.D. Lokhande, Big as well as light weight portable, Mn_3O_4 based symmetric supercapacitive devices: Fabrication, performance evaluation and demonstration, Electrochimica Acta 80 (2012) 160–170.

[26] D.P. Dubal, V.J. Fulari, C.D. Lokhande, Effect of morphology on supercapacitive properties of chemically grown β-$Ni(OH)_2$ thin films, Microporous and Mesoporous Materials 151 (2012) 511–516.

[27] D.P. Dubal, G.S. Gund, R. Holze, H.S. Jadhav, C.D. Lokhande, C.-J. Park, Surfactant-assisted morphological tuning of hierarchical CuO thin films for electrochemical supercapacitors, Dalton Transactions 42 (2013) 6459–6467.

[28] X. Xia, J. Tu, Y. Zhang, J. Chen, X. Wang, C. Gu, C. Guan, J. Luo, H.J. Fan, Porous Hydroxide Nanosheets on Preformed Nanowires by Electrodeposition: Branched Nanoarrays for Electrochemical Energy Storage, Chem. Mater. 24 (2012) 3793–3799.

[29] H. Chen, L. Hu, Y. Yan, R. Che, M. Chen, L. Wu, One-Step Fabrication of Ultrathin Porous Nickel Hydroxide-Manganese Dioxide Hybrid Nanosheets for Supercapacitor Electrodes with Excellent Capacitive Performance, Adv. Energy Mater. 3 (2013) 1636–1646.

[30] A.C. Nwanya, S.U. Offiah, C.I. Amaechi, S. Agbo, S.C. Ezugwu, B.T. Sone, R.U. Osuji, M. Maaza, F.I. Ezema, Electrochromic and electrochemical supercapacitive properties of Room Temperature PVP capped $Ni(OH)_2$/NiO Thin Films, Electrochimica Acta 171 (2015) 128–141.

[31] J.-K. Lee, H.M. Pathan, K.-D. Jung, Electrochemical capacitance of nanocomposite films formed by loading carbon nanotubes with ruthenium oxide, J. Power. Sources 159 (2006) 1527–1531.

[32] S.C. Pang, M.A. Anderson, T.W. Chapman, Novel electrode materials for thin-film ultracapacitors: Comparison of electrochemical properties of sol-gel-derived and electrodeposited manganese dioxide, J. Electrochemical Soc. 147 (2000) 444–450.

[33] C.-C. Hu, Y.-H. Huang, K.-H. Chang, Annealing effects on the physicochemical characteristics of hydrous ruthenium and ruthenium–iridium oxides for electrochemical supercapacitor, J. Power Sources 108 (2002) 117–127.

[34] X. Zhang, W. Shi, J. Zhu, D.J. Kharistal, W.Y. Zhao, B.S. Lalia, H.H. Hng, Q.Y. Yan, High-Power and High-Energy-Density Flexible Pseudocapacitor Electrodes Made from Porous CuO Nanobelts and Single-Walled Carbon Nanotubes, ACS Nano 5 (2011) 2013–2019.

[35] L. Yu, Y. Jin, L. Li, J. Ma, G. Wang, B. Geng, X. Zhang, 3D porous gear-like copper oxide and their high electrochemical performance as supercapacitors, CrystEngComm 15 (2013) 7657–7662.

[36] D.P. Dubal, G.S. Gund, R. Holze, C.D. Lokhande, Mild chemical strategy to grow micro-roses and micro-woolen like arranged CuO nanosheets for high performance supercapacitors, J. Power Sources 242 (2013) 687–698.

[37] D.P. Dubal, G.S. Gund, R. Holze, C.D. Lokhande, Enhancement in supercapacitive properties of CuO thin films due to the surfactant mediated morphological modulation, J. Electroanalytical Chemistry 712 (2014) 40–46.

[38] M.V. Reddy, C. Yu, F. Jiahuan, K.P. Loh, B.V.R. Chowdari, Molten salt synthesis and energy storage studies on $CuCo_2O_4$ and $CuO.Co_3O_4$, RSC Advances 2 (2012) 9619–9625.

[39] M.V. Reddy, G. Prithvi, K.P. Loh, B.V.R. Chowdari, Li Storage and Impedance Spectroscopy Studies on Co_3O_4, CoO, and CoN for Li-Ion Batteries, ACS Appl. Mater. Interfaces 6 (2014) 680–690.

[40] M.V. Reddy, C. Yu, F. Jiahuan, K.P. Loh, B.V.R. Chowdari, Li-Cycling Properties of Molten Salt Method Prepared Nano/Submicrometer and Micrometer-Sized CuO for Lithium, ACS Appl. Mater. Interfaces 5 (2013) 4361–4366.

[41] B. Varghese, Z. Hoong, M.V. Reddy, B.V.R. Chowdari, A.T.S. Wee, B.C. Tan Vincent, C.T. Lim, C.-H. Sow, Co_3O_4 Nanostructures with Different Morphologies and their Field-Emission Properties, Adv. Funct. Mater. 17 (2007) 1932–1939.

[42] G.S. Gund, D.P. Dubal, D.S. Dhawale, S.S. Shinde, C.D. Lokhande, Porous CuO nanosheet clusters prepared by a surfactant assisted hydrothermal method for high performance supercapacitors, RSC Advances 3 (2013) 24099–24107.

[43] A.C. Nwanya, C. Chigbo, S.C. Ezugwu, R.U. Osuji, M. Maaza, F.I. Ezema, Transformation of cadmium hydroxide to cadmium oxide thin films synthesized by SILAR deposition process: Role of varying deposition cycles, J. Association of Arab Universities for Basic and Applied Sciences (2014), doi: http://dx.doi.org/10.1016/j.jaubas.2014.09.001.

[44] C. Zhu, M.J. Panzer, Seed Layer-Assisted Chemical Bath Deposition of CuO Films on ITO-Coated Glass Substrates with Tunable Crystallinity and Morphology, Chem. Mater. 26 (2014) 2960–2966.

[45] A.D. Jagadale, V.S. Kumbhar, C.D. Lokhande, Supercapacitive activities of potentiodynamically deposited nanoflakes of cobalt oxide (Co_3O_4) thin film electrode, J. Colloid and Interface Science 406 (2013) 225–230.

[46] M.A. Chougule, S.G. Pawar, P.R. Godse, R.D. Sakhare, S. Sen, V.B. Patil, Sol–gel derived Co_3O_4 thin films: effect of annealing on structural, morphological and optoelectronic properties, J, Mater. Sci.: Mater Electron 23 (2012) 772–778.

[47] A. Amria, X.F. Duan, C.-Y. Yin, Z.-T. Jiang, M.M. Rahman, T. Pryor, Solar absorptance of copper–cobalt oxide thin film coatings with nano-size, grain-like morphology: Optimization and synchrotron radiation XPS studies, Applied Surface Science 275 (2013) 127–135.

[48] M. De Koninck, S.-C. Poirier, B. Marsan, $CuxCo3-xO4$ used as bifunctional electrocatalyst – Physicochemical properties and electrochemical characterization for the oxygen evolution reaction J, Electrochemical Society 153 (2006) A2103–A2110.

[49] J.C. Irwin, J. Chrzanowski, T. Wei, D.J. Lockwood, A. Wold, Raman scattering from single crystals of cupric oxide, Physcia C 166 (1990) 456–464.

[50] M.A. Dar, Q. Ahsanulhaq, Y.S. Kim, J.M. Sohn, W.B. Kim, H.S. Shin, Versatile synthesis of rectangular shaped nanobat-like CuO nanostructures by hydrothermal method; structural properties and growth mechanism, Appl. Surf. Sci. 255 (2009) 6279–6284.

[51] J. Zhao, R. Liu, Z. Hua, Hydrothermal synthesis and optical properties of single crystalline CuO nanosheets, Superlattices and Microstructures 81 (2015) 243–247.

[52] T. Yu, X. Zhao, Z.X. Shen, Y.H. Wu, W.H. Su, Investigation of individual CuO nanorods by polarized micro-Raman scattering, J. Crystal Growth 268 (2004) 590–595.

[53] J.S. Shaikh, R.C. Pawar, A.V. Moholkar, J.H. Kim, P.S. Patil, CuO–PAA hybrid films: Chemical synthesis and supercapacitor behavior, Applied Surface Science 257 (9) (2011) 4389–4397.

[54] D.P. Dubal, D.S. Dhawale, R.R. Salunkhe, V.S. Jamdade, C.D. Lokhande, Fabrication of copper oxide multilayer nanosheets for supercapacitor application, J. Alloys and compounds 492 (2010) 26–30.

[55] K.R. Prasad, N. Munichchandraiah, Electrochemical Studies of Polyaniline in a Gel Polymer Electrolyte: High Energy and High Power Characteristics of a Solid-State Redox Supercapacitor, Electrochemical Solid state letters 5 (2002) A271–A274.

[56] D. Patake, S.S. Joshi, C.D. Lokhande, O.-S. Joo, Electrodeposited porous and amorphous copper oxide film for application in supercapacitor, Mater. Chem. Phys. 114 (2009) 6–9.

[57] A.T. Chidembo, K.I. Ozoemena, B.O. Agboola, V. Gupta, G.G. Wildgoose, R.G. Compton, Nickel(II) tetra-aminophthalocyanine modified MWCNTs as potential nanocomposite materials for the development of supercapacitors, Energy Environ. Sci. 3 (2010) 228–236.

[58] V. Ganesh, S. Pitchumani, V. Lakshminnarayanan, New symmetric and asymmetric supercapacitors based on high surface area porous nickel and activated carbon, J. Power sources 158 (2006) 1523–1532.

[59] M. Moniruzzaman, S. Sahoo, D. Ghosh, C.K. Das, R. Singh, Preparation and Characterization of Polypyrrole/Modified Multiwalled Carbon Nanotube Nanocomposites Polymerized In Situ in the Presence Of BariumTitanate, J. Appl. Polym. Sci. 128 (2013) 698–705.

[60] D. Kalpana, Y.S. Lee, Y. Sato, New, low-cost, high-power poly(o-anisidine-co-metanilic acid)/activated carbon electrode for electrochemical supercapacitors, Journal of Power Sources 190 (2009) 592–595.

[61] R. Farma, M. Deraman, A. Awitdrus, I.A. Talib, E. Taer, N.H. Basri, J.G. Manjunatha, M.M. Ishak, B.N.M. Dollah, S.A. Hashmi, Preparation of highly porous binderless activated carbon electrodes from fibres of oil palm empty fruit bunches for application in supercapacitors, Bioresource Technology 132 (2013) 254–261.

[62] M. De la Fuente Salas, Y.N. Sudhakar, M. Selvakumar, High performance of symmetrical supercapacitor based on multilayer films of graphene oxide/polypyrrole electrodes, Applied Surface Science 296 (2014) 195–203.

[63] D.P. Dubal, G.S. Gund, C.D. Lokhande, R. Holze, CuO cauliflowers for supercapacitor application: Novel potentiodynamic deposition, Materials Research Bulletin 48 (2013) 923–928.

[64] D.P. Dubal, S.H. Lee, J.G. Kim, W.B. Kim, C.D. Lokhande, Porous polypyrrole clusters prepared by electropolymerization for a high performance supercapacitor, J. Materials Chemistry 22 (2012) 3044–3052.

[65] K. Raju, K.I. Ozoemena, Hierarchical One-Dimensional Ammonium Nickel Phosphate Microrods for High-Performance Pseudocapacitors, Scientific Reports 5 (2015) 17629.